Electromagnetic Analysis and Experimental Testing of a Flux Focusing Wind Turbine Magnetic Gearbox

Kang Li, *Student Member, IEEE*, Sina Modaresahmadi, *Student Member, IEEE*, Wesley Williams, Jonathan Bird, *Member, IEEE*, Jason Wright, *Student Member, IEEE*, David Barnett

***Abstract*—The electromagnetic design of the second stage of a 59:1 multistage magnetic gearbox for a wind turbine demonstrator is presented. The multistage series connected magnetic gearbox is composed of a 6.45:1 first stage and 9.14:1 second stage magnetic gear. The magnetic gears utilize a flux focusing spoke type rotor typology with a unique segmented fully laminated design. The electromagnetic impact of structural design changes on the second stage gearbox is considered with respect to torque density. Severe 3-D edge effects were encountered that greatly reduced the expect torque density of the stage 2 magnetic gear. Experimental testing of the multistage magnetic gear highlight unexpected problems associated with eddy current loss and torque ripple.**

***Keywords*—Gears, permanent magnet machines, magnetic flux density, magnetic forces, permanent magnets, torque**

I. Introduction

The most popular approach to converting a wind turbine's low-speed rotary motion into electricity is to utilize a doubly fed induction generator (DFIG) coupled to a mechanical gearbox. Currently, the majority of high-power wind turbines use this approach because the DFIG is low cost and the power electronic converter typically only needs to be sized to be around 30% of the rated power [1-3]. Unfortunately, wind turbine gearboxes have been one of the main causes of wind turbine down-time [4] and the gearbox failure rates increase with power level [4, 5]. This has resulted in the wind-turbine gearboxes not being able to achieve their desired 20 year design life [4, 6]. Furthermore, DFIGs utilize brushes which require regular maintenance which is difficult and expensive in many of the remote wind turbine site locations.

One of the main alternatives to the DFIG is the direct-drive (DD) permanent magnet (PM) generator which removes the reliability concerns regarding brushes and the mechanical gearbox. However, the torque density of a DD-PM generator is thermally limited (by current) and therefore a PM generator does not normally achieve torque densities greater than 50 Nm/L [7, 8]. For this reason DD-PM generators become very large when scaled-up in size [9, 10]. The increased size of the drivetrain also results in a significantly higher installation cost and therefore the system is then less cost competitive when compared with more traditional non-renewable energy sources or with the DFIG [11].

Magnetically geared generators [12-20] have recently been proposed as a way of increasing the wind-turbine drivetrain reliability without increasing the drivetrain size and therefore installation cost [18]. A magnetic gearbox (MG) enables speed amplification to be achieved without any mechanical contact, they do not require gear lubrication and they have inherent overload protection. As the losses are primarily frequency dependent they also have the potential to operate at a high conversion efficiency over a large loading range.

The coaxial MG is the most studied typology [21-25], an example of a flux-focusing coaxial MG typology is shown in Fig. 1. It consists of an inner rotor with p_1 pole pairs, an outer rotor with p_3 pole pairs and a central rotor made of n_2 ferromagnetic slots, termed a cage rotor in this paper. In order to maximize torque, the pole combination must satisfy

$$p_1 = n_2 - p_3 \tag{1}$$

and the outer rotor must be held stationary such that

$$\omega_3 = 0 \tag{2}$$

then the governing speed equation is given by [21]:

$$\omega_1 = G_{21} \cdot \omega_2 \tag{3}$$

where the gear ratio is

$$G_{21} = n_2 / p_1 . \tag{4}$$

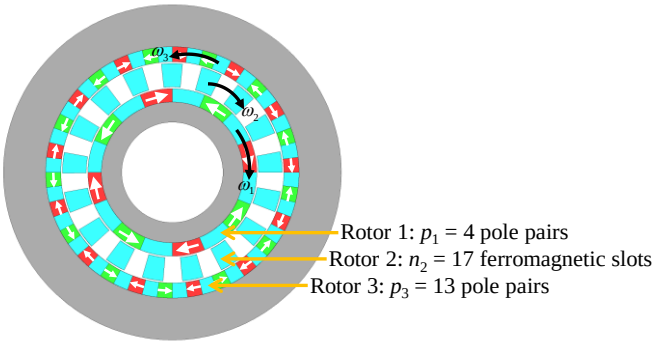

Fig. 1. An example of a coaxial flux-focusing magnetic gearbox.

Most analysis to-date has focused on using a wind turbine gear ratio that is less than 10:1 [12-20]. To achieve gear ratios comparable to their mechanical counterparts used in wind turbines a multistage MG is required.

This paper follows on from the analysis work presented in [19] the paper first summarizes the initial electromagnetic design analysis of the second stage MG [26] and then reports on the testing of the multistage series connected MG wind

This work was supported in part by the Department of Energy under grant number DE-EE0006801 and in part by a North Carolina Ocean Energy grant.
J. Z. Bird is a member of the Laboratory for Electromechanical Energy Conversion and Control, Portland State University, Portland, OR, 97201, USA. (email: jonathan.bird@ieee.org)
K. Li, S. Modaresahmadi, W. Williams, J. Wright and D. Barnett are with the University of North Carolina at Charlotte, Charlotte, NC, 28223, USA (email: wbwillia@uncc.edu)

turbine demonstrator. The gear ratio used for both stages is shown in Table I and an illustration of the two-stage design is shown in Fig. 2. The geometric and design information for the stage 1 MG is provided in [19]. The pole-pair combination of the stage 2 MG was selected as p_4 = 7, n_5 = 64 and p_6 = 57 this gives a stage 2 gear ratio of

$$G_{54} = n_5/p_4 = 9.\overline{142857} \quad (5)$$

As the outer and inner pole number is a prime number this minimizes torque ripple. When the stage 2 MG is connected in series to the stage 1 MG the total rotational speed equation becomes

$$\omega_4 = G_{21}G_{54}\omega_2 = 59.01\omega_2 \quad (6)$$

The 59:1 gear ratio was chosen to enable the multistage MG performance to be compared with the 59:1 Sumitomo cycloidal gearbox as shown in Fig. 3. The Sumitomo gearbox values and operating characteristics are summarized in Table II and III respectively. It should be noted that most high-power wind turbines use a planetary gearbox, and not a cycloidal gearbox, the Sumitomo gearbox was used as this high-torque gearbox was available to be used on the dynamometer test setup.

TABLE I
GEAR RATIOS USED FOR EACH STAGE OF THE COAXIAL MAGNETIC GEARBOX.

Stage 1	Inner rotor, p_1	11
	Cage rotor, n_2	71
	Outer rotor, p_3	60
	Gear ratio, G_{12}	$6.\overline{45}$
Stage 2	Inner rotor, p_4	7
	Cage rotor, n_5	64
	Outer rotor, p_6	57
	Gear ratio, G_{45}	$9.\overline{142857}$
Total gear ratio, $G_{12}G_{45}$		$59.\overline{012987}$

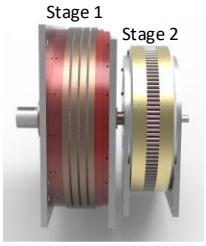

Fig. 2. Series connected stage 1 and stage 2 magnetic gearbox.

Fig. 3. Fanuc PM servo motor connected in series with a 59:1 Sumitomo cycloidal gearbox (CHHJ-4225Y-59-320TC). [27]

TABLE II
SUMITOMO CYCLOIDAL GEARBOX VALUES [27]

Parameter	Value	Units
Outer radius	275	mm
Active region axial length	210	mm
Total mass*	402.3	kg
Gear ratio, G_r	59	-

* This is the total mass.

TABLE III
SUMITOMO CYCLOIDAL GEARBOX OPERATING CHARACTERISTICS [27]

Operation Parameters	Output angular speed		Units
	1750 RPM	580 RPM	
Input rated, T_R	11.5	13.8	kN·m
Rated power ($T_R \cdot \omega_R$)	38.5	15.3	kW
Efficiency (at rated power)	93	93	%
Volume torque density	230	277	N·m/L
Mass torque density	28.6	34.2	N·m/kg

II. INITIAL MAGNETIC GEARBOX DESIGN

An initial stage 2 MG typology, called *Design I*, was first studied, this initial typology is shown Fig. 4. It uses a flux-focusing magnet arrangement and is based on the stage 1 design presented in [19]. The cage rotor is supported by central bridges and support rods. The geometric design and material parameters for *Design I* are given in Table IV. In this initial design the rotor airgaps were selected to be 0.5 mm and the axial length was set at 38.1 mm. A short axial length was selected in order to prevent the central cage rotor from deflecting. Using 2-D finite element analysis (FEA) the calculated active region volumetric torque density and torque were computed to be 375 Nm/L and 2719 Nm respectively. The volumetric torque density was computed from

$$T_{vd} = T_5 / (\pi r_{o6}^2 d) \quad (7)$$

where T_5 = torque on the low-speed cage rotor, r_{o6} = outer rotor radius and d = axial stack length.

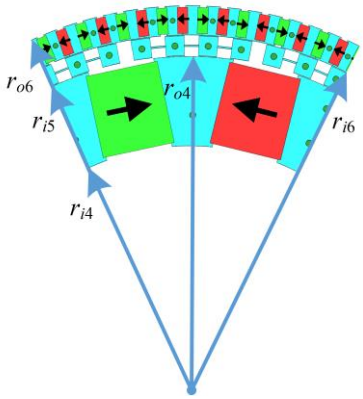

Fig. 4. Initial *Design I* version of the stage 2 flux focusing magnetic gearbox with a 0.5 mm air gap. [26]

Whilst proceeding with the stage 2 design serious deflection issues were encountered with the stage 1 laminated MG design, these deflection issues are discussed in [19]. Due to these issues a more robust stage 2 MG design was sort. However, as the inner rotor does not experience significant radial deflection force [19], and the inner rotor laminations were already fabricated, in the following analysis the inner rotor design will be unchanged from that shown in Fig. 4. Therefore, the inner rotor radial dimensions are kept fixed at (r_{i4}, r_{o4}) = (155, 213) mm.

It has been shown that the torque is maximized when the outer magnet angular span, θ_{6m}, and ferromagnetic steel pole span, θ_{6s}, are kept equal and also it has been found that the torque is maximized when the cage rotor angular span, θ_5, is equal to $\theta_5 \approx 2\theta_{6s}$ [28]. Therefore, with these angular span

constraints there are only two primary parameters that can be changed, they are the cage rotor length, defined as

$$l_5 = r_{o5} - r_{i5} \tag{8}$$

and the outer rotor length

$$l_6 = r_{o6} - r_{i6} \tag{9}$$

In the following sections the impact of varying these two key parameters, along with different structural design considerations will be studied with the aim of maximizing torque density.

TABLE IV
GEOMETRIC AND MATERIAL PROPERTIES FOR INITIAL AND FINAL STAGE 2 MAGNETIC GEARBOX DESIGN.

Description		*Design I* value	*Design V* value	Unit
Inner rotor	Inner radius, r_{i4}	155	155	mm
	Outer radius, r_{o4}	213	213	mm
	Radial magnet length	54	54	mm
	Magnet width, l_{im}	47.25	47.25	mm
Cage rotor	Inner radius, r_{i5}	213.5	214	mm
	Outer radius, r_{o5}	226.5	226	mm
Outer rotor	Inner radius, r_{i6}	227	227	mm
	Outer radius, r_{o6}	246	253.675	mm
	Radial magnet length, l_{om}	17	17	mm
	Magnet width	6.75	6.75	mm
Material	NMX-40CH, B_m	1.28	1.28	T
	M19 conductivity	0	0	S/m
	Steel rod 416 resistivity	57	57	μΩ-cm
Axial length, d		38.1	38.1	mm
Air gap, g		0.5	1	mm

III. IDEAL MAGNETIC GEARBOX DESIGN

To provide a baseline an ideal outer and cage rotor MG typology was first considered in which the airgaps were increased to 1 mm, this *Design II* is shown in Fig. 5. The airgap was increased in order to provide more tolerance robustness. To maximize torque density a 2-D FEA torque density analysis was conducted in which the cage rotor length was varied from l_5 = 7 mm to l_5 = 16 mm at 1 mm intervals and the outer rotor length was varied from l_6 = 15 mm to l_6 = 35 mm at 1 mm step intervals. The resultant torque density analysis plot for the 210 different simulation cases is shown in Fig. 6. The active region mass torque density shown on the *y*-axis was computed from

$$T_m = T_5 \,/\, (m_m + m_s) \tag{10}$$

where m_m = magnet material mass and m_s = lamination and support rod material mass. The radial length of the cage rotor, l_5, is shown in the legend of Fig. 6. Fig. 6 shows that a peak exists for maximizing volumetric torque density and this is at the expense of a non-optimal mass torque density. Table V gives a summary of the peak torque density values for each cage bar length, l_5. The peak volumetric torque density of 421 N·m/L occurred when (l_5, l_6) = (10, 22) mm.

IV. MAGNETIC GEARBOX WITH BRIDGE SUPPORTS

In order to increase the MGs structural strength *Design III* has a 1 mm bridge added on both radial sides of the cage rotor and outer rotor as shown in Fig. 7. The radial length of the cage rotor and outer rotor was then again varied. The resultant torque density analysis results are shown in Fig. 8 and Table VI. The bridges introduce significant additional flux leakage, as shown in Fig. 9, and this greatly reduce the peak torque density. From studying Table VI it can be noted that the peak volumetric torque density now occurs at (l_5, l_6) = (12, 24) mm and has reduced by 39 % to 256 N·m/L.

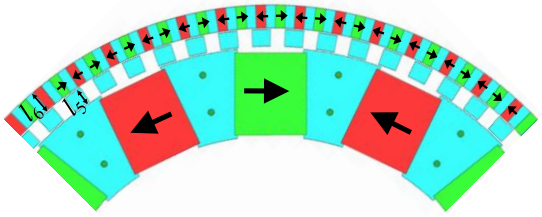

Fig. 5. Idealized *Design II* stage 2 magnetic gearbox with a 1 mm air gap. [26]

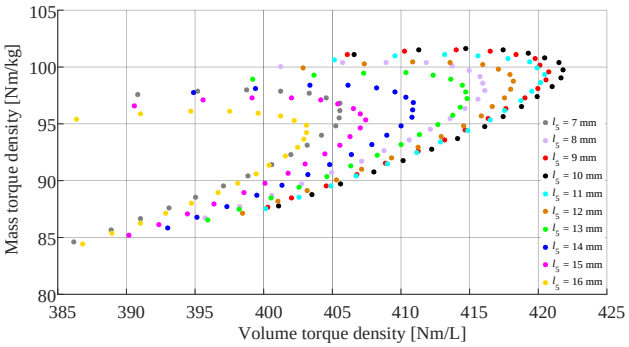

Fig. 6: Mass and volume torque density analysis plot when l_5 and l_6 were both varied for the idealized MG design. [26]

TABLE V
2-D CALCULATED PEAK TORQUE DENSITY AT RESPECTIVE CAGE BAR LENGTHS FOR *DESIGN II*

l_5 [mm]	l_6 [mm]	Volume torque density [Nm/L]	Mass torque density [Nm/kg]
7	21	405.5	96.8
8	23	416.1	97.9
9	22	420.7	99.6
10	22	421.8	99.8
11	22	420.5	99.4
12	22	418.2	98.7
13	23	414.8	97.2
14	22	410.9	96.9
15	23	407.4	95.3

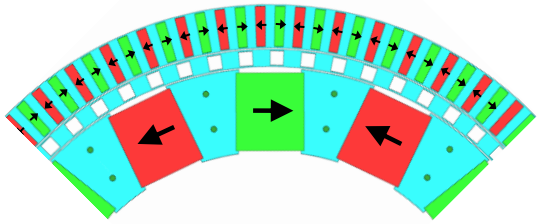

Fig. 7. Stage 2 MG *Design III* with 1 mm bridges on the cage and outer rotors. [26]

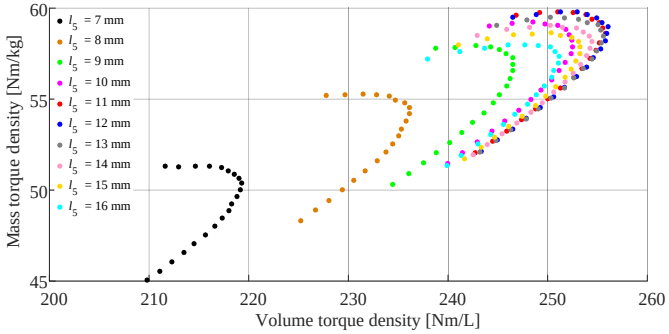

Fig. 8. Mass and volume torque density analysis plot for *Design III* when l_5 and l_6 were both varied for the MG bridge design. The length l_6 was varied from 17 mm to 37 mm at 1mm intervals. [26]

TABLE VI
PEAK TORQUE DENSITY AT RESPECTIVE CAGE BAR LENGTHS FOR *DESIGN III*

l_5 [mm]	l_6 [mm]	Volume torque density [Nm/L]	Mass torque density [Nm/kg]
7	25	219.3	50.4
8	25	236.2	54.2
9	25	246.5	56.6
10	25	252.5	57.9
11	25	255.8	58.6
12	24	256.1	59.0
13	25	255.6	58.5
14	25	254.4	58.2
15	26	253.2	57.5

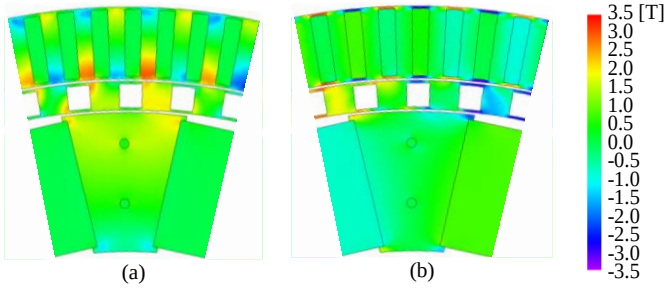

(a) (b)

Fig. 9. (a) Radial flux density B_r and (b) azimuthal flux density B_θ for the bridge support MG *Design III* when (l_5, l_6) = (12, 30) mm. The bridge leakage flux is clearly evident.

V. SEGMENTED BRIDGE SUPPORT DESIGN

In order to fabricate the laminated parts, the cage and outer rotor need to be segmented. The radial size makes it too large to manufacture the laminations as a single contiguous piece. Using the segmented *Design IV* typology shown in Fig. 10 the length analysis was repeated. The sweep analysis results for all length combinations are shown in Fig. 11. It can be noted that the peak torque density increases when compared to using bridges on all segments. Fig. 12 shows the torque vs. mass torque density and torque vs. volume torque density for the segmented design. From Fig. 12 it can be noted that the peak torque density does not occur at the peak torque value. This is because higher torque values are only achieved when the outer rotor radius, r_{o6} is increased. The peak volume torque density values for the different cage bar radial lengths, l_5, are summarized in Table VII. The peak volumetric torque density for *Design IV* is 302 N·m/L when (l_5, l_6) = (11, 25) mm.

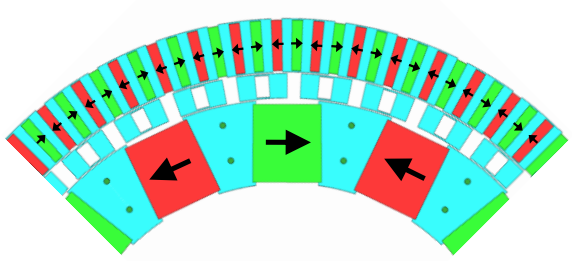

Fig. 10. Stage 2 magnetic gearbox with 1 mm bridges on the cage and outer rotors and segmented sections. [26]

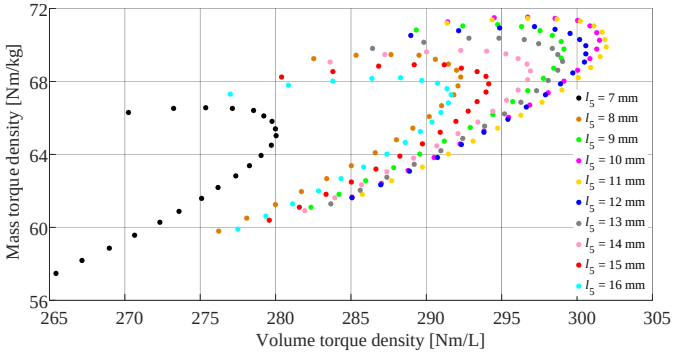

Fig. 11. Mass and volume torque density analysis plot for *Design IV* when l_5 and l_6 were both varied for the segmented bridge design. The length l_6 was varied from 17 mm to 37 mm. [26]

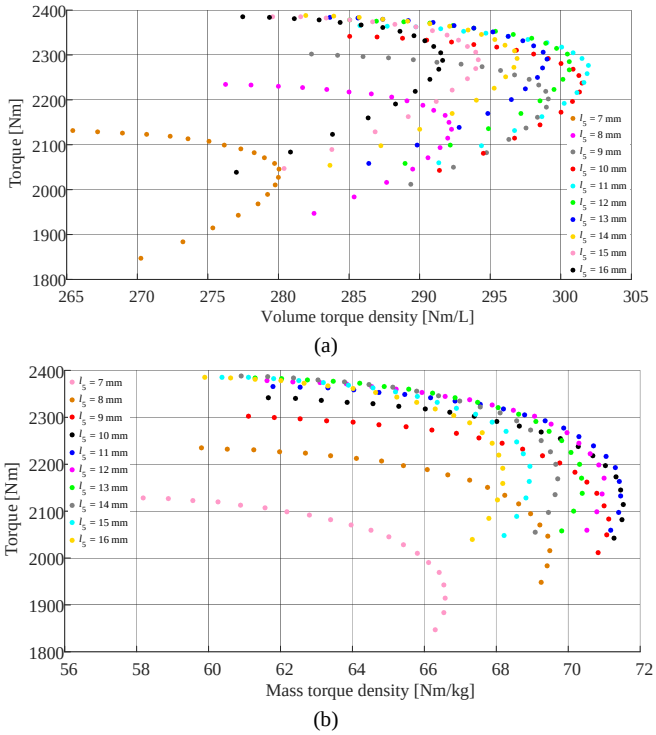

(a)

(b)

Fig. 12. (a) *Design IV* torque vs. volumetric torque density and (b) torque vs. mass torque density when l_5 and l_6 were varied. [26]

VI. FINAL MAGNETIC GEARBOX DESIGN

The difficulties encountered during the re-assembly of the stage 1 design [19] lead to the reassessment and invention of a new MG design approach. The outer rotor typology was again further modified to that shown in Fig. 13. The outer rotor is still supported by bridges on the inner radius like in

the prior design. However, the outer rotor radius now has support holes for retaining rods but no bridges. This design change mitigates some of the outer leakage flux whilst still providing mechanical support to both sides of the outer rotor. Furthermore, it moves the outer rotor support rods away from the air-gap thereby reducing eddy current loss within the rods. The reduction in outer radii leakage is evident in Fig. 14.

It should also be noted that in this final *Design V* the outer rotor radial length was reduced to enable existing outer magnets to be used which have a length of l_{om} =17 mm. A summary of the final MG design parameters is given in Table I. The 2-D calculated volume and mass torque density (with magnet grade N40 CH) was computed to be 232 Nm/L and 57 Nm/kg, respectively. The calculated torque ripple is low as shown in Fig. 15.

The 3-D model of the *Design V* MG is shown in Fig. 16. Unfortunately, the 3-D FEA showed that significant edge effects were created with this design and the calculated volume and mass torque density (with N40 CH magnets) reduced to just 124 N·m/L and 30 Nm/kg respectively. The field edge effects across the cross-section are clearly apparent in Fig. 17.

TABLE VII. TORQUE DENSITY VALUES FOR SEGMENTED BRIDGE *DESIGN IV*

l_5 [mm]	l_6 [mm]	Volume torque density [Nm/L]	Mass torque density [Nm/kg]
7	25	280.0	65.0
8	24	292.2	68.2
9	24	299.1	69.7
10	24	301.4	70.2
11	25	301.9	69.8
12	24	300.5	69.9
13	25	299.0	69.1
14	25	296.8	68.5
15	25	294.1	67.8

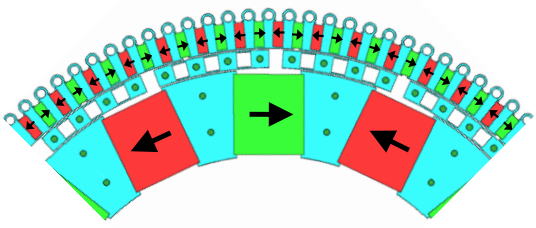

Fig. 13. Final *Design V* typology of the stage 2 MG.

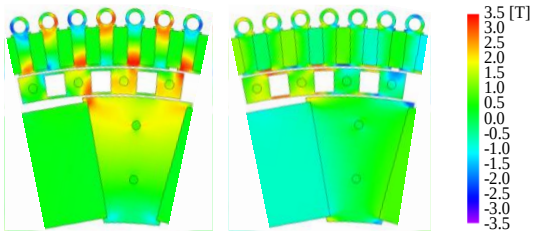

(a) (b)

Fig. 14. Surface plot of the (a) radial magnetic flux density, B_r and (b) azimuthal magnetic flux density, B_θ.

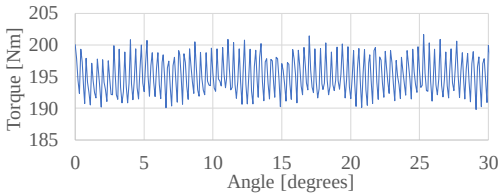

Fig. 15. (a) Calculated 2-D transient FEA torque on the high-high-speed inner rotor when neglecting losses. The ripple torque is created from the interaction of the higher order harmonics created by the flux-focusing rotors.

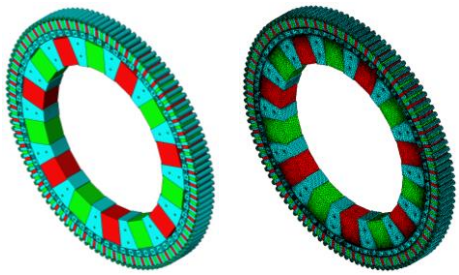

(a) (b)

Fig. 16. (a) 3-D FEA model and (b) mesh model. Due to the lack of symmetry a full 3-D model of the entire MG was required.

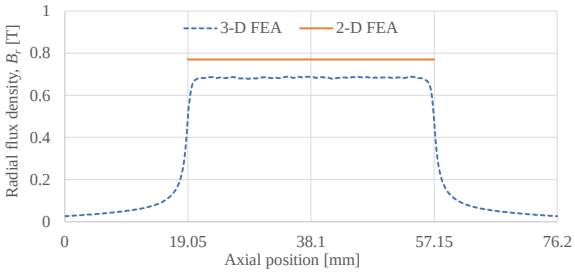

(a)

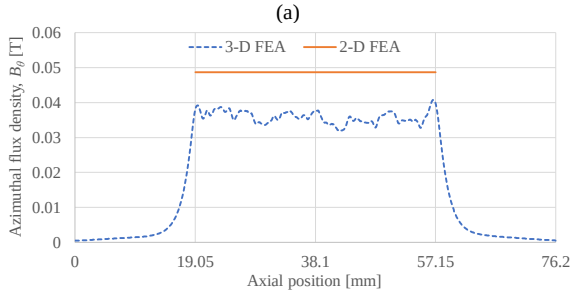

(b)

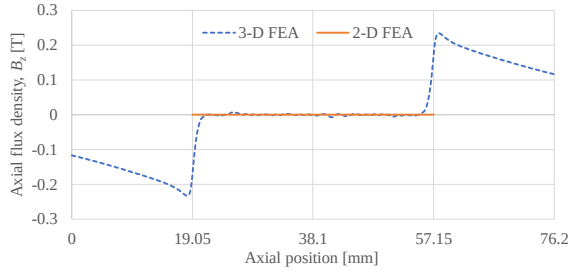

(c)

Fig. 17. (a) Radial (b) azimuthal and (c) axial magnetic field components along the axial length from 2-D and 3-D models. The values were calculated at r = 213.5 mm. The stage 2 MG region is from 19.05 mm to 57.15 mm.

VII. EXPERIMENTAL ASSEMBLY ANALYSIS

The mechanical assembly is shown in Fig. 18 and Fig. 19. When ordering the magnets, the magnet grade was chosen to be N45 SH. Therefore, this increased the 3-D calculated volume and mass torque density to 135 Nm/L and 33 Nm/kg. A

summary of the torque density for each of the discussed designs is provided in Table VIII.

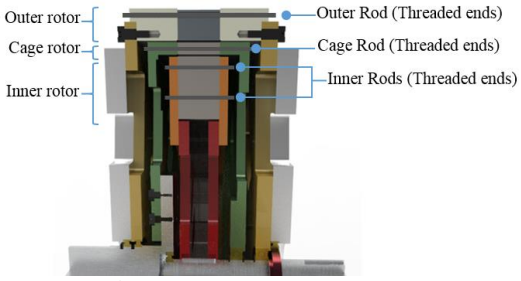

Fig. 18. Positioning of inner, cage and outer rotor connecting components of stage 2 MG.

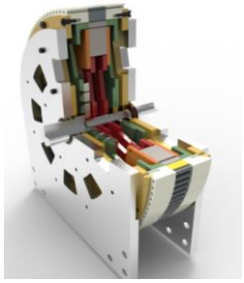

Fig. 19. A 90-degree cut-away view of the stage 2 MG showing all the interior mechanical components.

TABLE VIII
SUMMARY OF CALCULATED ACTIVE REGION TORQUE DENSITY

Design		FEA	Airgap [mm]	Radial length		Magnet grade	Peak torque [N·m]	Torque density	
Version	#			l_5	l_6			Volume [N·m/L]	Mass [N·m/kg]
Initial	*I*	2-D	0.5	13	9	N40	2719	375	90
Ideal	*II*	2-D	1	10	22	N40	3080	422	100
Bridges	*III*	2-D	1	12	24	N40	1931	256	59
Segmented	*IV*	2-D	1	11	25	N40	2277	302	70
Final	*V*	2-D	1	12	26.7	N40	1787	232	57
	V	3-D	1	12	26.7	N40	955	124	30
	V	3-D	1	12	26.7	N45	1040	135	33

The magnetic field on the inner and outer magnets was measured before inserting them and the field values were compared with the 3-D FEA model. The results are shown in Fig. 20 and indicate a good agreement. The inner, cage rotor and full assembly of the stage 2 MG is shown in Fig. 21. Due to machining cost considerations the end plates were made out of aluminium. The support rods were insulated with non-conductive inserts and non-conduct washers.

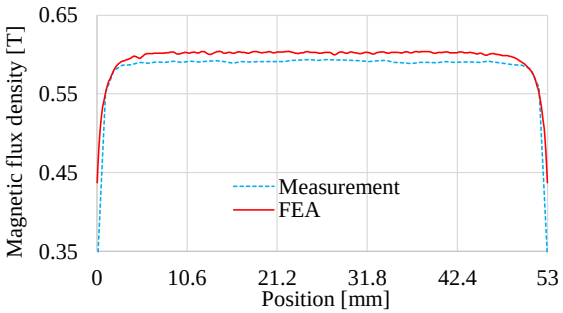

(a)

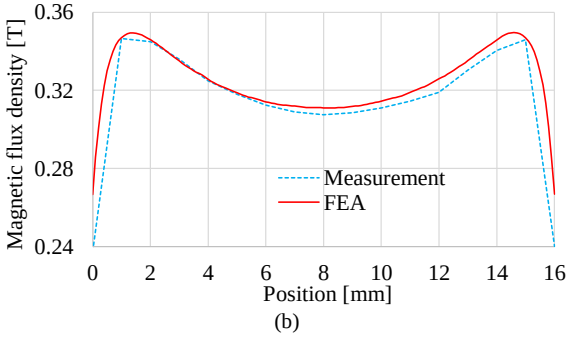

(b)

Fig. 20. Comparison of the (a) inner magnet and (b) outer magnet fields when measured along the radial direction at 0.54 mm above the surface.

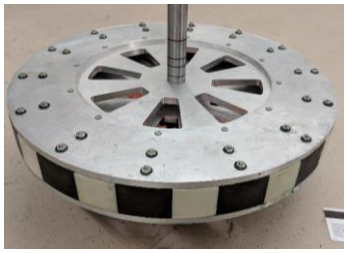

(a)

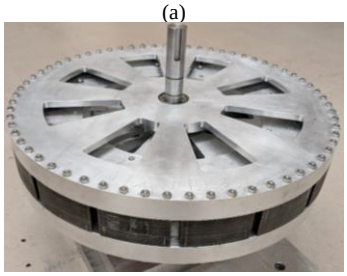

(b)

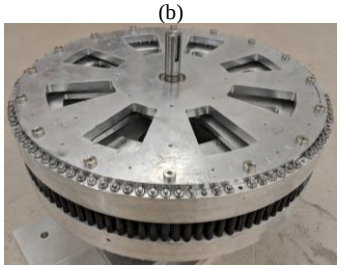

(c)

Fig. 21. Fully assembled (a) inner rotor (b) inner and cage rotors and (c) magnetic gearbox.

Before assembling the cage rotor, the radial magnetic flux density around the inner rotor was measured and compared with the 3-D FEA model. The comparison for one pole-pair is shown in Fig. 22 and the corresponding harmonic analysis is shown in Fig. 23. The flux-focusing typology results in a number of significant harmonics being created due to the non-sinusoidal field profile. The reduction in the magnitude due the 3-D edge effects is clearly apparent. The difference between the 2-D and 3-D fundamental harmonic is 64.6 %. However, the discrepancy in the fundamental field component between the measurement and 3-D FEA was only 1.42 %. The severe reduction in the field due to the edge effects demonstrates the importance of using 3-D FEA analysis when making radial sizing decisions.

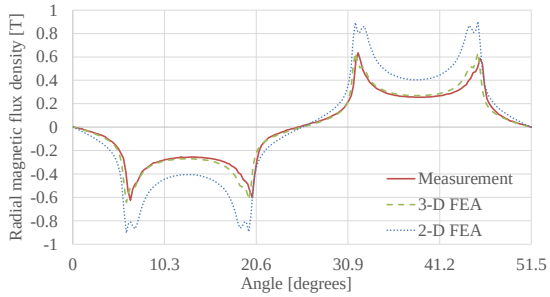

Fig. 22. The measured and FEA calculated radial magnetic flux density, B_r, at z = 20 mm and 0.66 mm above the rotor when the inner rotor is surrounded by air.

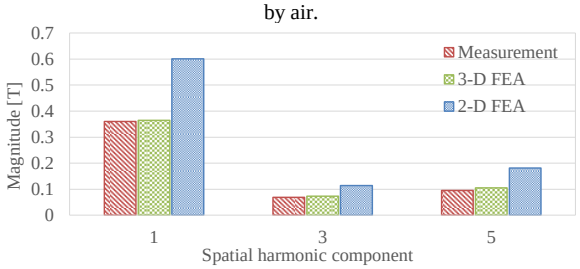

Fig. 23. Harmonic analysis comparison showing the 1st, 3rd and 5th harmonic for the measured and FEA calculated radial magnetic flux density for the inner rotor (when surrounded by air).

VIII. Experimental Test

The complete 59:1 multistage test setup is shown in Fig. 24. The low-speed input side of the stage 2 MG was connected to the high-speed output side of the stage 1 MG. The low-speed input side of the stage 1 MG was then connected to the 59:1 Sumitomo mechanical gearbox and a motor. Whilst the high-speed output side of the stage 2 MG was connected to a generator (and then an active front-end). Himmelstein torque transducers were used to measure the input and output torque and speed.

The testing of the multistage MG demonstrated that a very high output torque ripple was created as well as very large eddy current losses. For instance, when the input speed of the stage 1 MG was $\omega_1 = 0.01$ rad/s (0.92 RPM), the input and output torque were measured with an increasing applied load as shown in Fig. 25. It can be immediately seen in Fig. 25 that the output torque ripple is high and it does not change significantly with applied load. The torque ripple is independent of applied load and therefore if the torque ripple percentage is designed to be low at peak torque then unlike in a permanent magnet motor it will not scale down with applied torque. The torque ripple on the stage 2 MG is also compounded by the torque ripple from the stage 1 MG.

The efficiency was calculated to have a peak value of only 40% at full load. A significant amount of eddy current loss was created in the end-plates due to the field not being confined only to the active axial region. This splaying of the fields is seen in Fig. 17. The losses associated with the stage 1 MG and multistage MG can be seen in Fig. 26 for different input speeds and the higher losses due to the stage 2 MG is apparent. A thermal image showing the relative temperature difference on the outer end plates and inner end plates is shown in Fig. 27. This heating is at no-load and must be due to the eddy current eddy current losses. These eddy current losses could not be properly modelled because the computing resources available to the authors (128 GB RAM) were not sufficient to model such a large diameter non-symmetric problem in 3-D.

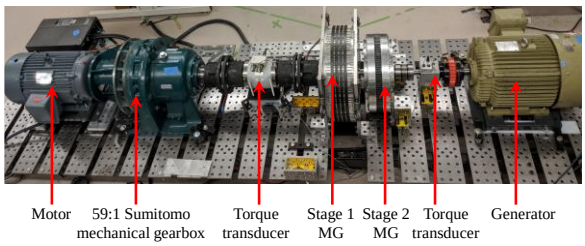

Fig. 24. Multistage magnetic gearbox test setup.

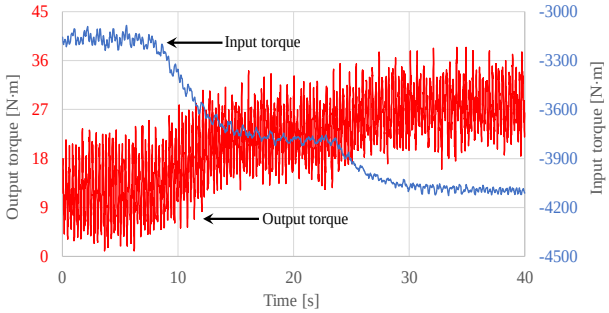

Fig. 25. Input and output torque at different load condition. The amount of losses within the stage 2 MG are severe and therefore result in the output torque being greatly reduced.

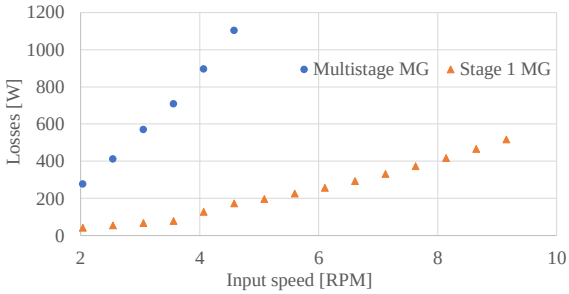

Fig. 26. Power loss as a function of input speed for the multistage magnetic gear as well as the stage 1 MG.

A performance comparison with the Sumitomo gearbox is shown in Table IX it can be seen that under all metrics the presented multistage MG falls short of the mechanical gear equivalent. Many of the reasons for the reduced torque density and increased loss are associated with making design assumptions that were based on smaller scaled MG prototypes. For example, the severity of the axial edge effects were not a focus of the design until changes could not be made. In addition, the non-sinusoidal field created by the flux focusing rotor typology along with the high number of poles creates a recipe for very high losses. Such losses are much less for lower pole designs. Based on the mechanical challenges associated with constructing the flux focusing outer rotor as well as the increase in harmonics created by the flux focusing design the authors have concluded that the use of a flux-focusing MG typology does not scale well. It is hoped that this paper will provide insight to future researchers on practical construction issues surrounding the design of large diameter MGs. A number of analytic based studies have demonstrated the potential scaling benefits, in terms of cost, of using

a magnetically geared generator for wind turbine use [29-31]. Further experimental prototypes as well as typology design studies need to be conducted in order to ascertain if using a series connected MG structure, as presented here, or using a nested structures as studied in [29-31] have the best potential for use in multi-MW wind turbine drivetrains. Whilst this paper has not focused on reducing the cost with respect to magnet usage other studies, such as presented in [32] and [15] have indicated that by using magnetic gearing a comparable amount of magnet material as a direct-drive generator will be needed. The cost saving of using magnetic gearing will therefore come from using significantly less magnetic steel, copper and reducing the structural costs associated with having a smaller outer diameter.

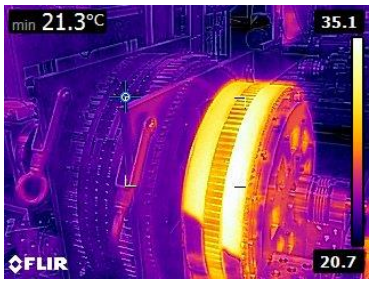

(a)

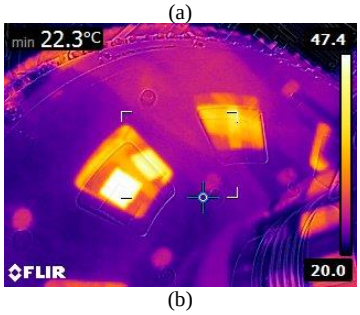

(b)

Fig. 27. Thermal imaging of the multistage magnetic gear during no-load operation. The heating of the stage 2 outer end plates in (a) as well as inner rotor end plates in (b) are evident.

TABLE IX
MAGNETIC GEAR PERFORMANCE COMPARISON WITH THE SUMITOMO CYCLOIDAL GEARBOX

Parameter	Sumitomo cycloidal gearbox	Multistage magnetic gearbox	Units
Outer radius	275	316.5*	mm
Active region axial length	210	114.5‡	mm
Total mass*	402.3	303.3‡	kg
Gear ratio, G_r	59	59	-
Peak rated torque	13.8†	4.25	kN·m
Active region volume torque density	277	118	N·m/L
Structural mass torque density	34.2	14	N·m/kg

* This is outer radius of the stage 1 MG
† at 580 RPM
‡ Value is for both stages

IX. CONCLUSIONS

The electromagnetic FEA design analysis for a flux focusing MG is described along with the experimental fabrication and test results of a 59:1 multistage MG. The stage 2 MG torque density was calculated to be 135 N·m/L and the multistage MG torque density was measured to be only 118N·m/L. The mass and volumetric torque density as well as efficiency of the MSMG did not meet the original target values. This was due to a number of factors, such as the 3-D edge effects being more severe than expected as well as the need for support rings on the stage 1 MG. The experimental testing showed that the eddy current losses were much more severe than expected and this is believed to be due to the high harmonic content created by the flux-focusing rotor typology as well as the eddy current losses induced in the end plates and support rods. The electrical losses and torque ripple are not load dependent and therefore this resulted in the MSMG having an extremely low efficiency at light load with an excessively large output torque ripple at all torque conditions. It is hoped that the presented results will help future researchers avoid some of the short comings identified in the presented design.

ACKNOWLEDGMENTS

The authors would gratefully like to thank the JMAG Corporation and ANSYS Corporation for the use of their FEA software. This work was supported in part by the Department of Energy under grant number DE-EE0006801 and in part by a North Carolina Ocean Energy grant.

REFERENCES

[1] S. Muller, M. Deicke, *et al.*, "Doubly fed induction generator systems for wind turbines," *IEEE Ind. Appl. Mag.*, vol. 8, pp. 26-33, 2002.
[2] F. Wang, Y. Zhang, *et al.*, "Comparison of different structures for variable speed constant frequency wind power generation," in *Int. Conf. Elect. Mach. Sys.*, Wuhan, China, 2008, pp. 2234-2238.
[3] H. Li and Z. Chen, "Overview of different wind generator systems and their comparison," *IET Renew. Power Gener.*, vol. 2, pp. 123-138, 2008.
[4] W. Musial, S. Butterfield, *et al.*, "Improving Wind Turbine Gearbox Reliability," National Renewable Energy Laboratory, NREL/CP-500-41548, May 2007.
[5] S. Sheng and P. Veers, "Wind turbine drivetrain condition monitoring - an overview," in *MFPT: Applied Systems Health Management Conference*, Virginia Beach, VA 2011.
[6] J. V. Rensselar, "The elephant in the wind turbine," *Tribology Lubrication Technology*, vol. June, pp. 2-12, 2010.
[7] M. R. J. Dubois, "Optimized Permanent Magnet Generator Topologies for Direct-Drive Wind Turbines," Ph.D. Thesis, Delft University of Technology, Delft, Netherlands, 2004.
[8] T. J. E. Miller, *Brushless Permanent-Magnet and Reluctance Motor Drives*: Oxford University Press, 1989.
[9] P. Kasinathan, A. Grauers, *et al.*, "Force density limits in low-speed permanent-magnet machines due to saturation," *IEEE Trans. Energy Conv.*, vol. 20, pp. 37-44, Mar. 2005.
[10] D. G. Dorrell, S. S. Ngu, *et al.*, "Comparison of high pole number ultra-low speed generator designs using slotted and air-gap windings," *IEEE Trans. Mag.*, vol. 48, pp. 3120-3123, Nov. 2012.
[11] H. Polinder, F. F. A. Van der Pijl, *et al.*, "Comparison of direct-drive and geared generator concepts for wind turbines," *IEEE Trans. Energy Conv.*, vol. 21, pp. 725-733, 2006.
[12] L. Jian, K. T. Chau, *et al.*, "A magnetic-geared outer-rotor permanent-magnet brushless machine for wind power generation," *IEEE Trans. on Ind. Appl.*, vol. 45, pp. 954-962, 2009.
[13] N. W. Frank and H. A. Toliyat, "Gearing Ratios of a magnetic gear for wind turbines," presented at the IEEE Elect. Mach. Drive Conf., Miami, FL, May 3-6, 2009.
[14] M. Desvaux, R. L. G. Latimier, *et al.*, "Design and optimization of magnetic gears with arrangement and mechanical constraints for wind turbine applications," presented at the Eleventh Inter. Conf. Eco. Veh. Renew. Energies, Monaco, Monaco, Apr. 2016.
[15] A. Penzkofer, "Analytical Modelling and Analysis of Magnetic Gears and Pseudo Direct Drives for Large Wind Turbines," Ph.D. thesis, Electrical and Computer Enginering, University of Sheffield, 2016.

[16] L. Jian, G. Xu, *et al.*, "Electromagnetic design and analysis of a novel magnetic-gear-integrated wind power generator using time-stepping finite element method," *Progr. Electrmagn. Res.*, vol. 113, pp. 351-367, 2011.
[17] K. S. Belkhir and N. Khenfer, "Magnetic gear generator for wind energy," *Przegald Elektrotechniczny* vol. 5, p. 72, 2013 2013.
[18] R. Wang and S. Gerber, "Magnetically geared wind generator technologies: opportunities and challenges," *Applied Energy*, vol. 136, pp. 817-826, 2014.
[19] K. Li, J. Wright, *et al.*, "Designing the first stage of a series connected multistage coaxial magnetic gearbox for a wind turbine demonstrator," in *2017 IEEE Energy Conversion Congress and Exposition (ECCE)*, 2017, pp. 1247-1254.
[20] G. Q. Bao and K. F. Mao, "A wind energy conversion system with field modulated magnetic gear," presented at the Asia-Pacific Power and Energy Engineering Conference, Wuhan, China, 2011.
[21] T. B. Martin, "Magnetic Transmission," USA Patent 3,378,710, 1968.
[22] P. O. Rasmussen, T. O. Andersen, *et al.*, "Development of a high-performance magnetic gear," *IEEE Transactions on Industry Applications*, vol. 41, pp. 764-770, 2005.
[23] K. Atallah, S. D. Calverley, *et al.*, "Design, analysis and realisation of a high-performance magnetic gear," *IEE Proceedings - Electric Power Applications*, vol. 151, pp. 135-143, 2004.
[24] K. K. Uppalapati, W. B. Bomela, *et al.*, "Experimental Evaluation of Low-Speed Flux-Focusing Magnetic Gearboxes," *IEEE Transactions on Industry Applications*, vol. 50, pp. 3637-3643, 2014.
[25] D. Som, K. Li, *et al.*, "Analysis and Testing of a Coaxial Magnetic Gearbox With Flux Concentration Halbach Rotors," *IEEE Transactions on Magnetics*, vol. 53, pp. 1-6, 2017.
[26] K. Li, S. Modaresahmadi, *et al.*, "Electromagnetic Analysis of a Wind Turbine Magnetic Gearbox," presented at the The 9th Intern. Conf.Power Elect. Mach. Drives, Liverpool, UK, 2018.
[27] K. Li and J. Z. Bird, "Scaling equations for an axial magnetic coupling," *Submitted to IEEE Trans Magn.*, 2016.
[28] K. K. Uppalapati, W. Bomela, *et al.*, "Experimental Evaluation of Low Speed Flux Focusing Magnetic Gearboxes," *IEEE Trans. on Ind. Appl.*, vol. 50, pp. pp. 3637 – 3643, Nov/Dec 2014.
[29] A. B. Abrahamsen, D. Liu, *et al.*, "Final assessment of superconducting (SC) and Pseudo Direct Drive (PDD) generator performance indicators," INNWIND.EUOct. 2018.
[30] S. K. Moore, "The Troubled Quest for the Superconducting Wind Turbine," *IEEE Spectrum*, 26 Jul. 2018.
[31] A. Penzkofer and K. Atallah, "Analytical modeling and optimization of pseudo-direct drive permanent magnet machines for large wind turbines," *IEEE Trans. Magn.*, vol. 51, pp. 1-14, Dec. 2015.
[32] S. Gerber and R.-J. Wang, "Torque capability comparison of two magnetically geared PM machine topologies," in *IEEE International Conference on Industrial Technology*, Cape Town, South Africa, Feb. 25-28, 2013, pp. 1915-1920.